UCRL-JRNL-205051

MHD Simulation of the Inverse Pinch Plasma Discharge

A. Esaulov, B.S. Bauer, I. Lindemuth, V. Makhin, R. Presura, D. Ryutov, P. Sheehey, R. Siemon, V. Sotnikov

September 23, 2003

Physics of Plasmas

This document was prepared as an account of work sponsored by an agency of the United States Government. Neither the United States Government nor the University of California nor any of their employees, makes any warranty, express or implied, or assumes any legal liability or responsibility for the accuracy, completeness, or usefulness of any information, apparatus, product, or process disclosed, or represents that its use would not infringe privately owned rights. Reference herein to any specific commercial product, process, or service by trade name, trademark, manufacturer, or otherwise, does not necessarily constitute or imply its endorsement, recommendation, or favoring by the United States Government or the University of California. The views and opinions of authors expressed herein do not necessarily state or reflect those of the United States Government or the University of California, and shall not be used for advertising or product endorsement purposes.

This work was performed under the auspices of the U.S. Department of Energy by University of California, Lawrence Livermore National Laboratory under Contract W-7405-Eng-48.

MHD simulation of the inverse pinch plasma discharge

A. Esaulov, B. S. Bauer, I. Lindemuth[†], V. Makhin, R. Presura, D. Ryutov[‡]
P. Sheehey[†], R. Siemon, V. Sotnikov
Physics Department, University of Nevada, Reno, NV 89557
[†]*Los Alamos National Laboratory, Los Alamos, NM 87545*
[‡]*Lawrence Livermore National Laboratory, Livermore, CA 94550*

September 23, 2003

Abstract

A wall confined plasma in an inverse pinch configuration holds potential as a plasma target for Magnetized Target Fusion (MTF) as well as the simple geometry to study wall-confined plasma. An experiment is planned to study the inverse pinch configuration using the Nevada Terawatt Facility (NTF) at the University of Nevada, Reno (UNR). The dynamics of the discharge formation have been analyzed using analytic models and numerical methods. Strong heating occurs by thermalization of directed energy when an outward moving current sheet (the inverse pinch effect) collides with the outer wall of the experimental chamber. Two dimensional MHD simulations show Rayleigh–Taylor and Richtmyer–Meshkov -like modes of instability, as expected because of the shock acceleration during plasma formation phase. The instabilities are not disruptive, but give rise to a mild level of turbulence. The conclusion from this work is that an interesting experiment relevant to wall confinement for MTF could be done using existing equipment at UNR.

PACS numbers: 52.65.Kj, 52.58.Lq, 52.50.Lp, 52.35.Py

1 Introduction

For the Magnetized Target Fusion (MTF) approach to fusion, a desirable plasma target before the high-energy compression phase would typically have density 10^{24} m^{-3}, temperature 300 eV, $\beta \sim 1$ ($\beta = 2\mu_0 p/B^2$ is ratio of plasma pressure to magnetic field pressure), and energy confinement time exceeding the compression time, typically 10 μs [1, 2, 3]. These parameters are experimentally nontrivial, and the optimum method for achieving them has not been determined [3]. One approach involves direct support of plasma pressure by material boundaries [4]. The possibility of wall confinement has been discussed at length theoretically [5, 6], but wall confinement has been studied relatively little experimentally.

The key issues for wall confinement involve the interaction between the material wall and the high-temperature plasma. How rapidly the plasma cools throughout the volume, and how quickly the wall material mixes with fusion fuel are the main concerns. According to theory, thermal insulation is significantly improved perpendicular to a magnetic field provided the plasma is magnetized in the sense that ion $\omega\tau \gg 1$, where ω is the cyclotron frequency, and τ is the collision time. When a room-temperature boundary holds finite plasma pressure, a very dense sheath of plasma develops near the wall. For a given pressure, density increases as the temperature goes down towards the wall because of thermal conduction. The sheath structure is complicated with very different transport properties in different regions. The structure has been described using classical transport estimates [5], but turbulence is likely to develop and result in non-classical transport. Large enhancements over Bremsstrahlung radiation can also be expected from the dense sheath as impurities mix from the wall.

Wall confinement is a quite complex issue, and experiments will be required to evaluate its potential. A pioneering experiment was done by Feinberg at Columbia University in the 1970s [7]. It provided evidence that thermal transport agrees with classical theory. The present day MAGO experiment at VNIIEF in Russia is investigating wall confinement for MTF targets in a regime of high energy density [8]. This paper will describe a lower-energy-density experiment focused on the physics of wall-plasma interactions, which is planned at the UNR. It will utilize the Zebra hardware at the Nevada Terawatt Facility [9].

The desired conditions of temperature and $\omega\tau$ needed for MTF targets require a considerable amount of heating, which is provided by shock heating in all the wall-confined experiments just mentioned. Classical Ohmic heating would be negligible in a pulsed high-beta plasma leaning on a wall. In other words, the characteristic Ohmic heating time would be much longer than the energy confinement time under such conditions. Relatively fast losses of heat to the walls is acceptable in an MTF context because theoretically the losses can be overcome by the fast compression.

The inverse pinch geometry was selected for the NTF experiment because of its well known shock heating capability

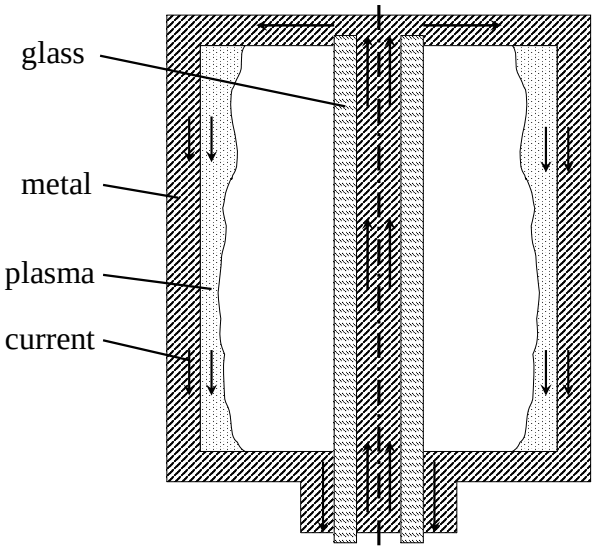

Figure 1: An inverse pinch geometry to heat and hold plasma against a room-temperature wall. Plasma from the uniform gas-fill is initially accelerated outward by a current sheet that forms on the glass insulator because of fast-rising current. Plasma then settles into an equilibrium with $\mathbf{j} \times \mathbf{B} = \nabla p$ throughout the volume and with finite pressure on the boundaries.

in addition to its favorable field line curvature for MHD stability. The geometry is shown schematically in Fig. 1. The generic features are:

1. A slow-rising current to provide a bias level of magnetic field before the discharge begins.
2. A dynamic phase with rapidly rising current that forces a current sheet outward from the insulator.
3. A thermalization phase after the current sheet encounters the outer boundary, involving multiple reflections of shock waves that convert directed energy into thermal energy.
4. An equilibrium phase where magnetized plasma is held against the outer boundary by the magnetic field from current that is presumed to be held constant on the inner conductor.

Only the final equilibrium phase is shown schematically in Fig. 1.

The original term "inverse pinch" comes from Furth and colleagues [10]. They and others [11, 12] were primarily interested in the plasma acceleration and shock heating processes. The inverse pinch geometry has proven useful as a plasma accelerator for space applications [13], as a source of electromagnetic radiation [14], and as a neutron source [15, 16].

Not much discussion can be found in the literature concerning the confinement properties of an inverse pinch during the equilibrium phase. The only example to our knowledge is the MAGO configuration that involves two chambers and two current sheets. One current sheet accelerates plasma axially through a nozzle-like construction, while another current sheet forms on an insulator and propagates outward as in an inverse pinch.

The new experiment at UNR would differ from MAGO by using a single chamber with good diagnostic access. A lower-energy-density regime should allow high repetition rate of the experiment. The goal is to understand the intrinsic confinement properties of the wall-confined inverse pinch with the geometry as simple as possible.

In the 1960s an experiment called an "inverse pinch" investigated a linear geometry that combined axial B_z field with axial current flowing through electrodes [17, 18]. Electron thermal conduction in the axial direction parallel to $\mathbf{B}$ limited the temperature to about 50 eV, but the configuration had features similar to an inverse pinch in the radial direction. Density around 10^{21} m^{-3} and interesting lifetimes over 100 μs were reported. We prefer to use the term "inverse pinch" to specify purely axial current and azimuthal B_θ field that drives a current sheet radially outward at early time. On the time scale of interest, the magnetic field should remain parallel everywhere to the conducting boundaries.

This paper is devoted mainly to the dynamic phase of plasma formation. Section 2 describes the Zebra experimental facilities at the NTF facility. Section 3 describes the MHRDR code used for numerical simulations. In Section 4 the plasma acceleration and thermalization phase are discussed using results from one-dimensional numerical simulations compared with the standard snowplow model and other analytic expressions. In Section 5, the magneto-acoustic oscillations around equilibrium seen in one-dimensional simulations are described, and Kadomtsev's criterion [19] for MHD stability of a given equilibrium is summarized. Section 5 also includes a discussion of MHD model applicability. Section 6 compares 1D MHRDR simulations with recent experimental results [15, 16] reported by the Institute of High Current Electronics (Tomsk, Russia) for their inverse pinch experiment. Finally, Section 7 describes instabilities seen in 2D simulations with the MHRDR code. Rayleigh-Taylor type instabilities are seen in simulations that have seeded perturbations, or in simulations that lack axial uniformity because of room-temperature electrodes.

2 NTF experimental parameters

The 2 TW Zebra [9] pulsed-power device is a refurbished pulse-power system originally operated as a high-density z-pinch at Los Alamos National Laboratory [20]. For application to an inverse pinch, a front end that resembles Fig. 1 would be fabricated to serve as the electrical load for the 2 MV, 1 MA electrical generator. The dimensions of the discharge chamber for the inverse pinch modeled in this paper

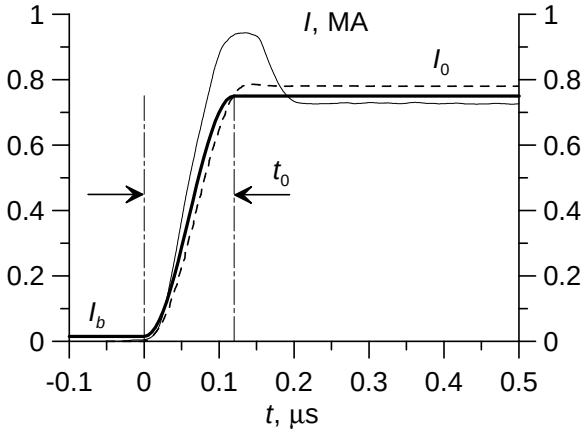

Figure 2: Typical experimental load current in Zebra (thin line) and SCREAMER calculations for inverse pinch (dashed line). Idealized waveform used for numerical calculations (bold line) consists of bias current I_b, current rise-time t_0, and peak current I_0 level.

are: axial length $l_z = 30$ cm, inner radius $R_I = 2$ cm, outer radius $R_W = 10$ cm. The inductance for such a load would almost be a short circuit for the generator, and the maximum output current at full voltage would be approximately 1 MA rising in 150 ns.

Similar electrical loads have been used on the existing apparatus, and a usual feature of the discharges is an automatic crowbar of current near its peak. The crowbar is caused by a repeatable flashover of the insulator on the Zebra output where power feeds to the vacuum transmission line carrying current to the experimental load. The flashover occurs shortly after peak current when voltage reverses on the insulator.

Circuit analysis for the inverse pinch geometry has been carried out using the SCREAMER code [21] in the approximation that load inductance does not change with the time. The predicted discharge current waveform is shown in Fig. 2, along with the experimental waveform obtained when using similar impedances, and the idealized current waveform used for numerical modeling. Three values characterize the idealized waveform: bias current I_b, rise-time t_0, and peak current I_0. The initial level of current, which we term the "bias current" requires an additional power supply on the Zebra facility. The bias current can be introduced with a low-voltage capacitor bank isolated from the Marx generator with a large inductor.

The high-voltage generator can be operated in different modes, which affect the peak current I_0 and rise time t_0, by adjusting the spacing of electrodes in the water switches. The highest–power mode is shown in Fig. 2. A reduced–power mode results from smaller electrode spacing. For the same initial charge voltage, the reduced-power mode has about half the current and double the rise time. The advantage of the reduced–power mode is more reliable operation and faster turn-around time between pulses.

3 Method of numerical simulation

A numerical code called MHRDR (Magneto-Hydro-Radiative-Dynamics-Research) will be used for these investigations. This code has been developed by I. Lindemuth and P. Sheehey at Los Alamos National Laboratory. The MHRDR code simulates dynamics of hot, dense, magnetized plasma in 2D, using the MHD approximation. The MHD equations are integrated numerically, assuming cylindrical symmetry of the plasma configuration. And only plasma dynamics in (r, z)-plane and only azimuthal component of the magnetic field $\mathbf{B} = \mathbf{e}_\theta B$ are considered. The implicit in time numerical scheme with an adjustable time step is used for the integration. The MHRDR computer code works with one-, two- and three- temperature (ion T_i, electron T_e, and radiation) plasma models.

3.1 Basic equations of MHD model

The MHD model considers the following set of the equations for evolutions of the mass density ρ, bulk velocity $\mathbf{v}$, specific internal energy for ion ε_i and electron ε_e components of plasma, and magnetic field intensity B:

$$\frac{\partial \rho}{\partial t} + \nabla \cdot (\rho \mathbf{v}) = 0 \ , \tag{1}$$

$$\frac{\partial (\rho \mathbf{v})}{\partial t} + \nabla \cdot (\rho \mathbf{v} \otimes \mathbf{v}) + \nabla p + \frac{1}{\mu_0} \mathbf{B} \times (\nabla \times \mathbf{B}) = 0 \ , \tag{2}$$

$$\frac{\partial \mathbf{B}}{\partial t} - \nabla \times (\mathbf{v} \times \mathbf{B}) + \frac{1}{\mu_0} \nabla \times (\eta \nabla \times \mathbf{B}) = 0 \ , \tag{3}$$

$$\frac{\partial (\rho \varepsilon_i)}{\partial t} + \nabla \cdot (\rho \mathbf{v} \varepsilon_i) + p_i \nabla \cdot \mathbf{v} + \nabla \cdot (\kappa_\perp^i \nabla T_i) - Q_{ei} = 0 \ , \tag{4}$$

$$\frac{\partial (\rho \varepsilon_e)}{\partial t} + \nabla \cdot (\rho \mathbf{v} \varepsilon_e) + p_e \nabla \cdot \mathbf{v} + \nabla \cdot (\kappa_\perp^e \nabla T_e) - \\ - \frac{\eta}{\mu_0^2} (\nabla \times \mathbf{B})^2 + Q_{ei} + Q_{rad} = 0 \ . \tag{5}$$

Kinetic transport coefficients in transverse magnetic field η, $\kappa_\perp^i$, $\kappa_\perp^e$ and electron ion heat exchange term Q_{ei} have been calculated by using Braginskii formulas [22].

The simulations in this paper use the simplified model of one-temperature ($T_e = T_i$) completely ionized plasma and only Bremsstrahlung radiation is included into the radiation cooling term Q_{rad}.

3.2 Initial conditions

Simulations were performed in a rectangular (r, z)-domain that represents the discharge chamber, shown on Fig. 1, with inner radius $R_I = 2$ cm, outer radius $R_W = 10$ cm, and axial

length $l_z = 30$ cm. It will be supposed that the discharge chamber is filled uniformly with deuterium. The initial mass density of the fill gas is chosen to be $\rho = 5 \times 10^{-6}$ kg/m^3, which corresponds to the background pressure of of $p_b \approx$ 23 mtorr for the molecular deuterium.

The results discussed in this paper assumes the reduced–power mode: $I_0 = 500$ kA and $t_0 = 200$ ns. Under such conditions one should expect the magnetic field energy to be $W_M \sim 10$ kJ, and voltage drop between the electrodes of the discharge chamber to be $V \sim 100$ kV. Two values of the bias current, $I_b = 15$ kA and 25 kA, are considered in order to reveal the influence of the trapped magnetic flux on pressure profile in the vicinity of the outer wall. The majority of 1D simulation results will be obtained for $I_b = 15$ kA. Then, in Section 5 the results for both these values of I_b will discussed. 2D simulations will be performed for $I_b = 25$ kA.

4 Shock acceleration and heating

The initial slow-rising bias current does not create current in the static gas fill. When high voltage is applied to generate the main current pulse, a current sheet would be expected to form in an experiment along the insulator by ionization and Ohmic heating of the gas fill. In simulations the ionization process is approximated by starting with a 2–mm thick layer of 1 eV plasma adjacent to the insulator. The Lorentz force accelerates the current sheet outward (inverse pinch effect) producing a strong shock wave driven by the magnetic piston through the background gas.

According to modeling and consistent with many experiments, the current sheet can be approximated as a perfect conductor for the time scale of radial motion. The increasing flux associated with the applied high voltage is contained in the region between the inner conductor and the current sheet, and the initial bias flux in the region between the current sheet and the outer conductor stays nearly constant, giving rise to increased magnetic field strength as the current sheet approaches the outer boundary.

The evolution and structure of the current sheet and shock wave are shown in Fig. 3.

4.1 Snowplow model of shock acceleration

The simplified snowplow model assumes the plasma accretion is performed at the thin layer with the mass M that is adjacent to the current sheet. Acceleration occurs due to the action of the magnetic field pressure:

$$\frac{d}{dt}(Mu) = 2\pi r l_z p_m = \frac{\mu_0}{4\pi}\frac{l_z}{r} I^2 \ , \qquad (6)$$

where r is the position of the current sheet, $u = dr/dt$ is its velocity, and I is the electric current in circuit. The mass of the accreted plasma behind the shock wave front is expressed as $M = \pi\left(r^2 - R_I^2\right) l_z \rho$. Thus, the dynamics of the

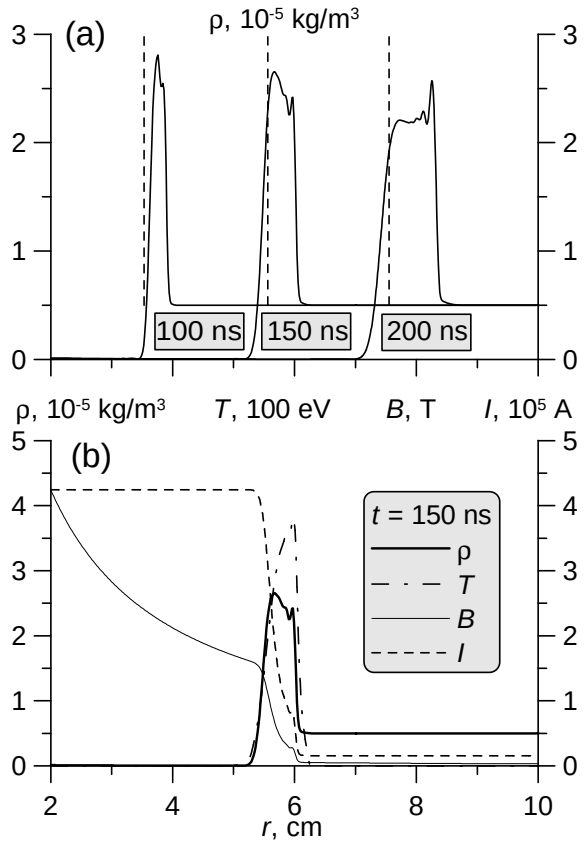

Figure 3: Shock wave driven by the magnetic piston. Graph (a) presents density profiles at three different moments: $t =$ 100, 150 and 200 ns. Vertical dotted lines represent the position of the current sheet as predicted by the snowplow model. Graph (b) shows the structure of the shock wave: profiles of the density ρ, temperature T, magnetic field B and the enclosed electric current I at $t = 150$ ns.

shock acceleration can described by the following differential equation:

$$r\frac{d}{dt}\left[\left(r^2 - R_I^2\right)\frac{dr}{dt}\right] = \frac{\mu_0}{4\pi^2}\frac{I^2}{\rho} \ . \qquad (7)$$

Voltage drop between the electrodes U is one of the important experimental parameters, which can be estimated in the snowplow model as follows:

$$U = \frac{\partial}{\partial t}\iint_S B dr dz = \frac{\mu_0}{2\pi} l_z \left[\frac{dI}{dt}\ln\left(\frac{r}{R_I}\right) + \frac{I}{r}\frac{dr}{dt}\right] \ . \qquad (8)$$

The predictions made by the snowplow model are compared with MHRDR calculations on Figs. 3 and 4. Dynamic equation (7) gives us a set of the scaling laws for shock parameters like velocity u, kinetic energy per unit length $K_l = Mu^2/(2l_z)$, and average energy per particle $k = m_i u^2/2$:

$$u \sim \frac{I_0}{2\pi R_W}\sqrt{\frac{\mu_0}{\rho}} \ ; \quad K_l \sim \frac{\mu_0 I_0^2}{8\pi} \ ; \quad k \sim \frac{\mu_0}{8\pi^2}\frac{I_0^2 m_i}{R_W^2 \rho} \ , \qquad (9)$$

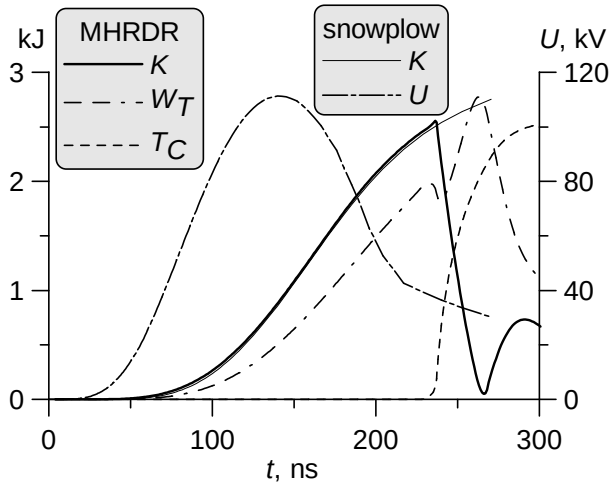

Figure 4: Simulation results by MHRDR computer code: kinetic energy K, thermal energy W_T, energy lost due to the thermal conduction T_C (all in kJ units). Predictions by snowplow model: kinetic energy of the shock wave K, kJ; and the inductive voltage drop between the electrodes U, kV [Eq. (8)]. Time scale in the figure corresponds to the dynamic phase and the first hit against the wall.

where m_i is the ion mass. As we can see, the total kinetic energy of the shock is determined by the shape of the current profile. Yet the energy per particle (i.e. resultant temperature of plasma) is inversly proportional to the specific mass of the fill gas per unit length in axial direction.

In the limit $R_I/R_W \ll 1$ Eq. (7) responds with an asymptotic solution $r = R_W(t/t_0)^{\frac{n+1}{2}}$ for the current waveform $I = I_0(t/t_0)^n$. It gives the following expressions for temporal evolution of shock parameters for two specific shapes of the current pulse: linearly rising current $I \propto t$

$$r \propto t \ , \quad u = \text{const} \ , \quad K_l \propto t^2 \ , \quad k = \text{const} \tag{10}$$

and constant current $I = \text{const}$

$$r \propto \sqrt{t} \ , \quad u \propto \frac{1}{\sqrt{t}}, \quad K_l = \text{const} \ , \quad k \propto \frac{1}{t} \ . \tag{11}$$

4.2 Thermalization of directed energy

During the dynamic stage the shock wave moves with the velocity u, which is hypersonic (≈ 150 Mach) with respect to the parameters of filling gas. Such a shock causes rapid plasma compression at the shock wave front. Plasma parameters behind the shock wave front (denoted below with subscript "1") can be calculated for a plane shock wave moving with constant velocity. In this case one can use the exact solution for very strong shock $p_1 \gg p_b$ ($\gamma = 5/3$ is below):

$$p_1 = \frac{\gamma+1}{2}\rho u^2 = \frac{4}{3}\rho u^2 \ , \quad \rho_1 = \frac{\gamma+1}{\gamma-1}\rho = 4\rho \ . \tag{12}$$

Thermal energy W_T, accumulated behind the shock wave front in this approximation, will be exactly the same as the kinetic energy K:

$$W_T = \frac{1}{\gamma-1}\iiint p_1 dV = \frac{\gamma+1}{\gamma-1}\frac{\rho}{\rho_1}\frac{Mu^2}{2} = K \ . \tag{13}$$

As we can see from the data in Fig. 4 for cylindrical shock wave accumulated thermal energy is less than the kinetic energy $W_T \leq K \approx 2.5$ kJ.

When the plasma collides with the outer wall, the major part of the kinetic energy is transformed to the internal energy of the plasma. One might expect doubling of the thermal energy, but the heat loss to the outer wall due to thermal conduction is substantial as shown in Fig. 4. Therefore, the thermal energy does not much exceed the level obtained before plasma collides with the wall. Later in time thermal energy gradually decays as heat flows to the cold outer wall on a microsecond time scale.

5 Relaxation to equilibria in 1D

After the first hit against the outer wall the shock wave experiences multiple reflections between the outer solid and inner magnetic boundaries. As shown in Fig. 5, the intensity of the shock wave goes down together with the remains of kinetic energy, and the plasma motion gradually converts to magnetoacoustic oscillations. When the radial motion damps out, the expected equilibria between magnetic and plasma pressure are observed. Because of thermal conduction perpendicular to B, the thermal energy confinement time for the conditions specified in Section 3 is about 10 μs.

5.1 Oscillations about equilibria

The equilibrium plasma state of a diffuse z-pinch is uniform along z, and the balance of $\mathbf{j} \times \mathbf{B}$ and ∇p

$$\frac{\partial p}{\partial r} + \frac{\mu_0}{8\pi^2}\frac{1}{r^2}\frac{\partial}{\partial r}(I^2) = 0 \tag{14}$$

has well known solutions and features [19].

Experimental measurement of plasma energy losses is often accomplished in high-β experiments by measuring the decay of plasma diamagnetism. In a one-dimensional equilibrium, that is, with variations only in the radial direction, magnetic measurements external to the high-temperature plasma can be related to thermal energy per unit length in either the ordinary z-pinch or the θ-pinch configuration. The technique might be useful for an inverse pinch, although two complications arise: pressure is finite at the outer wall, and magnetoacoustic oscillations might complicate the measurement.

For the inverse pinch geometry considered here, the thermal energy W_T between two radii $r = a$ and $r = b$ can be

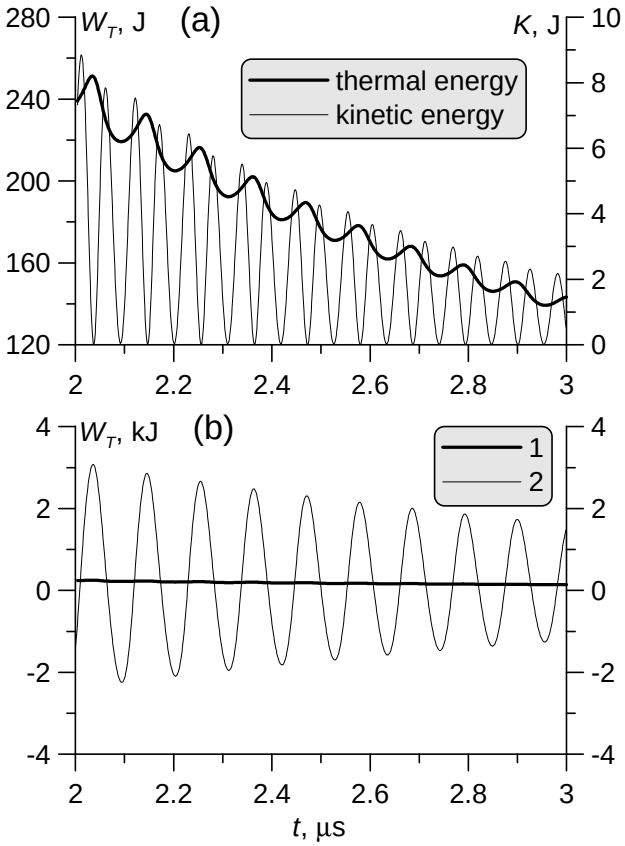

Figure 5: Graph (a) shows damping of the oscillations of thermal W_T and kinetic K energies of plasma according to numerical simulations. Graph (b) compares the corrected value of thermal energy W_T (curve 1) given by Eq. (18) with an estimate for a static equilibrium (curve 2), using Eq. (15).

expressed from Eq. (14):

$$W_T = \frac{3}{2}\iint_a^b p 2\pi r dr dz = l_z \delta \left[\frac{3\pi}{2} r^2 p + \frac{3\mu_0}{16\pi} I^2\right] , \qquad (15)$$

where $I = (2\pi/\mu_0) rB$, and $\delta[f(r)] = f(b) - f(a)$. By placing magnetic probes at radii a and b that surround essentially all of the plasma energy, the desired measurement of thermal energy vs. time could be made. However, it would be necessary to measure both B and p at the outer wall (typically $p(R_I)R_I^2/p(R_W)R_W^2 \ll 1$) for the conditions of interest in an inverse pinch. Direct electrical measurements of p might be possible [23], and a measurement of B at the wall and at small radius where pressure is negligible, and probe pertubations should be minimal, should be straightforward with magnetic probes.

A diagnostic approach based on the above logic is further complicated by magnetoacoustic oscillations. In one-dimensional simulations, oscillations are observed to persist throughout the thermal cooling time. Following the dynamic phase described in Section 4, the kinetic energy damps out relatively quickly, and one might have expected an equilibrium relationship like Eqs. (14)–(15) above to apply. Instead numerical simulations show oscillations around the equilibrium as indicated in Figs. 5 and 6. The frequency of the oscillations appear to be related to the magnetoacoustic frequency f_m:

$$t_m = \frac{1}{f_m} = \frac{2\Delta r}{\sqrt{c_A^2 + c_S^2}} \qquad (16)$$

For a thickness $\Delta r = 5$ mm if we choose $\rho = 10^{-4}$ kg/m^3, $p = 10^5$ Pa and $B = 1$ T, then we have the following: Alfven velocity $c_A \approx 9 \times 10^4$ m/s, sound velocity $c_S \approx 4 \times 10^4$ m/s. So, one expects a frequency $t_m \sim 100$ ns and the numerically observed frequency is 106 ns at $t = 3\mu s$.

The modification of the equilibrium relationship by the oscillations can be seen in detail by integrating the equation of motion with inertial terms included

$$\frac{\partial}{\partial t}(\rho v) + \frac{1}{r}\frac{\partial}{\partial r}(r\rho v^2) + \frac{\partial p}{\partial r} + \frac{\mu_0}{8\pi^2}\frac{1}{r^2}\frac{\partial}{\partial r}(I^2) = 0 \qquad (17)$$

rather than just equilibrium Eq. (14). In that case,

$$W_T = l_z \delta \left[\frac{3\pi}{2} r^2(\rho v^2 + p) + \frac{3\mu_0}{16\pi} I^2\right] - \\ -\frac{3}{2}K + \frac{3\pi}{2} l_z \frac{\partial}{\partial t}\int_a^b \rho v r^2 dr \ . \qquad (18)$$

At times like that depicted in Fig. 5, $K/W_T \ll 1$. It means that the kinetic energy of plasma motion is negligible compared to the other terms of Eq. (18). And within the solid boundaries we have $\delta[r^2\rho v^2] = 0$. Yet, surprisingly, the influence of the inertia term $\partial/\partial t$ in the right-hand side of the equation (18) is not negligible, and the definition, given by Eq. (15), contains a large oscillating error vs. Eq. (18) [see Fig. 5(b)].

5.2 Hydromagnetic stability at equilibrium

According to the Kadomstev criteria [19], hydromagnetic stability of the plasma against the sausage $m = 0$ mode at equilibrium [Eq. (14)] depends on the shape of the pressure profile. For ideal gas $\gamma = 5/3$:

$$-\frac{d\ln p}{d\ln r} < \frac{20}{6 + 5\beta} \ . \qquad (19)$$

Thus, a plasma equilibrium is unconditionally stable if plasma pressure increases with the radius (as at the inside interface between plasma and magnetic field), and can be stable if plasma pressure drops sufficiently slowly towards the outer boundary.

Plasma pressure at the wall always becomes large for a brief time during the stage of thermalization of the directed energy, but then drops to a smaller and variable amount as radial oscillations damp out and equilibrium is established. Pressure profiles seen in Fig. 6 are oscillating near the equilibria. They are formed as expected with large gradients of

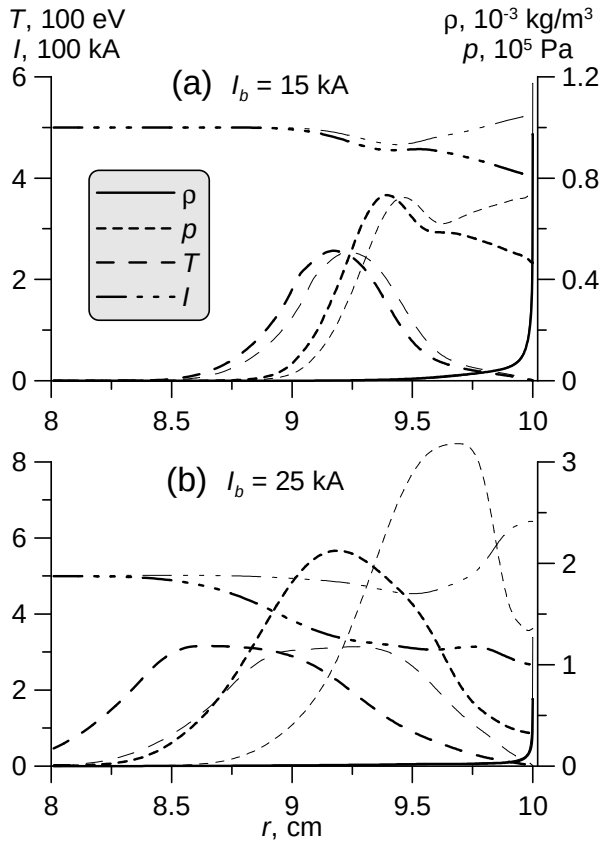

Figure 6: Radial plasma oscillation near the equilibrium at $t \approx 3\mu s$, depending on the value of bias current I_b. Radial profiles for plasma parameters: mass density ρ, 10^{-3} kg/m^3, pressure p, 10^5 Pa, temperature T, 100 eV and electric current I, 10^5 A are shown at two consecutive moments of time that correspond to the minimum (solid lines) and maximum (thin lines) of plasma thermal energy.

plasma temperature and density at the cold wall. The characteristic width of this boundary layer is defined by the thermal conduction of plasma and can be estimated from the data, shown in Fig. 6, as $\delta r_\kappa \sim 0.5$ cm.

After formation of a high-conductivity plasma layer along the surface of the inner electrode, the magnetic flux becomes trapped between the current sheet and the outer wall. The value of the trapped magnetic flux Φ_B is directly proportinal to the total enclosed electric current $I_1(t)$ $[I_1(0) = I_b]$ at the outer edge of the current sheet:

$$\Phi_B = \iint_S B dr dz = \frac{\mu_0}{2\pi} I_1(t) l_z \ln\left(\frac{R_W}{r_p(t)}\right) , \qquad (20)$$

where $r_p(t)$ is the position of the current sheet. Neglecting magnetic field diffusion, the value Φ_B is constant in time. The last assumption allows us to estimate the equilibrium value of $r_p = R_p$. In approximation of the thin current sheet, $I_1 \approx I_0$, so Eq. (20) gives:

$$R_p = R_W \left(\frac{R_I}{R_W}\right)^{I_b/I_0} \qquad (21)$$

Being compressed by the outward moving current sheet, the trapped magnetic flux causes large magnetic pressure that finally stops the current sheet as it approaches the outer wall. Bias magnetic field also provides thermal insulation. However, the pressure profile created with this field is unstable in the region between the maximum pressure and the outer wall according to the Kadomtsev stability criterion. Using the notation of Ref. [6] the criterion (19) can be written as $Q < 1$ where

$$Q = -\frac{d\ln p}{d\ln r} \cdot \frac{6+5\beta}{20} . \qquad (22)$$

For the case of $I_b = 15$ kA, $Q_{\max} \sim 5$, where $Q_{\max}$ is the maximum value of Q as a function of radius. When $I_b = 25$ kA, the criterion is violated by an even larger factor: $Q_{\max} \sim 20 - 30$. Even in a case with zero bias current and the same fill density, the substantial amount of the magnetic field diffuses through the current sheet and then gets compressed by the sheet motion giving $Q_{\max} \sim 3$. By changing both fill pressure and bias current a few examples were found with $Q_{\max} < 1$ at early times following equilibration. But in all cases the pressure profile changed after a few microseconds because of diffusion and thermal conduction and then showed $Q_{\max} > 1$. These simulations suggest that some additional method of plasma control will be needed to create Kadomtsev-stable pressure profiles.

The frequency of the magneto-acoustic radial oscillations is also dependent on the value of bias current. If $I_b = 15$ kA Eq. (21) gives the following estimation: $\Delta r = R_W - R_p \approx 0.5$ cm. It means that almost all plasma forms the boundary layer adjacent to the outer wall $\Delta r \approx \delta r_\kappa$.

If $I_b = 25$ kA, a noticeable part of the plasma with typical density $\rho \approx 2 \times 10^{-4}$ kg/m^3 is located out of boundary layer: $\Delta r \approx 0.8$ cm. Simulations then show an increased period for magneto-acoustic oscillations, $t_m \approx 145$ ns, and Eq. (16) gives $t_m \approx 144$ ns.

The features of 1D plasma dynamics, described in this Section, are fully applicable for 2D plasma configuration, providing the system is uniform in axial direction. On the other hand, axial non-uniformity may change the character of plasma dynamics after the formation stage. This issue will be discussed in details in Section 7.

5.3 Applicability of the MHD model

The gyro radii for the electrons ρ_{Be} and ions ρ_{Bi}

$$\rho_{Ba} = \frac{v_{Ta}}{\omega_{Ca}} , \ \omega_{Ca} = \frac{Z_a e B}{m_a} , \ v_{Ta} = \sqrt{\frac{3T_a}{m_a}} , \ a = e, i \qquad (23)$$

Table 1: Averaged plasma parameters in the vicinity of the outer wall for the cases $I_b = 15$ kA and $I_b = 25$ kA

r, cm	9		9.5		9.9
I_b, kA	15	25	15	25	15&25
ρ, kg/m^3	10^{-7}	10^{-6}	10^{-5}	2×10^{-5}	10^{-4}
T, eV	150	300	100	170	15
B, T	1.1	1.1	1	0.8	0.9
ρ_{Be}, cm	10^{-3}	10^{-2}	10^{-3}	10^{-2}	10^{-3}
ρ_{Bi}, cm	0.3	0.4	0.3	0.4	0.1
λ_{ei}, cm	400	100	7	8	10^{-2}
$\omega_{Ce}\tau_e$	10^5	10^4	10^3	10^3	14
$\omega_{Ci}\tau_i$	400	80	7	5	0.06

and their lengths of mean free path $\lambda_{ei} = v_{Te}\tau_e$ and $\lambda_{ii} = v_{Ti}\tau_i$ (see, for example, Ref. [22])

$$\frac{1}{\tau_e} = \frac{\sqrt{2}}{3\sqrt{\pi}}\frac{\mu_0^2}{4\pi}\frac{(ce)^4}{\sqrt{m_e}}\Lambda_{ei}\frac{Zn_e}{T_e^{3/2}}\ ,\ \frac{1}{\tau_i} = \frac{\mu_0^2}{4\pi}\frac{(ce)^4}{\sqrt{m_i}}\Lambda_{ii}\frac{Zn_e}{T_i^{3/2}} \quad (24)$$

are given in Table 1. The electrons are strongly magnetized: $\omega_{Ce}\tau_e \gg 1$. However, ions are magnetized in the vicinity of boundary layer: $\omega_{Ci}\tau_i \gg 1$ at $r \le 9.5$ cm, and are non-magnetized $\omega_{Ci}\tau_i \ll 1$ at the boundary layer $r > 9.5$ cm that is adjacent to the outer wall.

The mean free path of the electrons and ions dramatically changes from the center to the outer wall: $\lambda \propto (T^2/\rho)$. At hot low-density region of plasma $r \le 9$ cm both ions and electrons are practically collisionless $\lambda/R_W \gg 1$. Electron MHD approximation still can be used provided that the mean total displacement of the electron for the time between two consecutive collisions is small vs. the typical plasma size: $\lambda_{ei} \ll R_W^2/\rho_{Be}$ in the cylindrical configurations with pure toroidal magnetic field [26]. Under some assumptions the dynamics of collisionless ions still can be considered in MHD approximation [27]. Yet in the latter case one should take into account two–fluid effects due to the strong Hall term and the effects of the anomalous transport in low-density plasmas.

The extreme case of low-density plasma has been discussed above. The MHD model, considered in this paper, is still applicable even in such conditions. Yet some problems may arise due to the lack of plasma collisionality. The magnetic field pressure that supports plasma at the inside interface is defined by the value of peak current I_0 and the position of the current sheet at equilibrium R_p. At the same time the value of plasma β basically is the function of bias current I_b and the fill pressure p_b. Over a wide range of parameters relevant to the UNR experiment $\beta \sim 20-50\%$, which means that the plasma pressure $p = nT$ remains approximately constant as initial gas pressure is varied. So, the higher density of the inverse pinch plasma can be "traded" for its lower temperature; thus the collisionality of plasma can be substantially increased: $\lambda \propto (T^2/\rho) \propto p^2/\rho^3$.

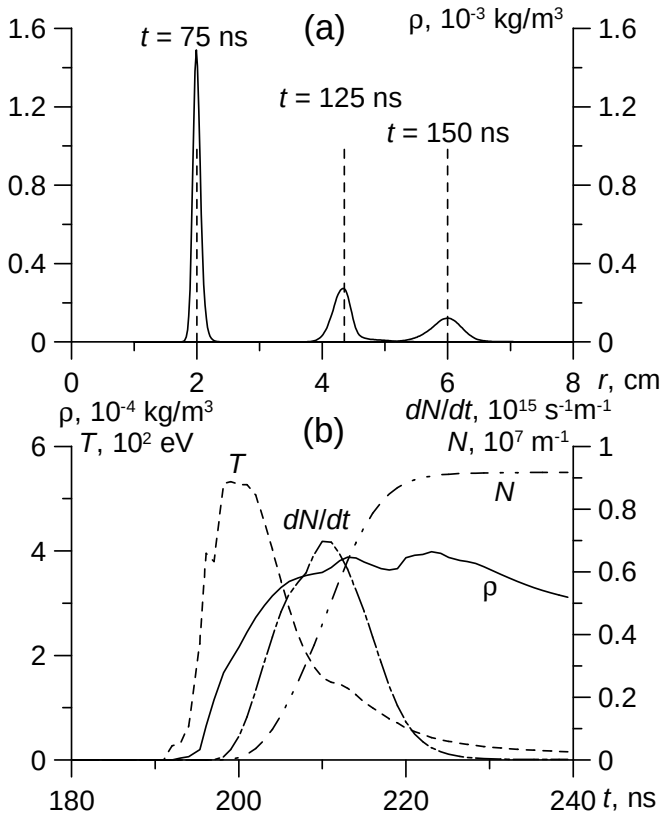

Figure 7: 1D simulation of the Tomsk inverse pinch experiment. Graph (a) presents the evolution of the density profile during liner acceleration (solid lines represents simulation results due to MHRDR code; dotted lines denote current sheet position inferred from the magnetic probes). Graph (b) shows MHRDR simulations data for the evolution of mass density ρ and temperature T near the wall ($R_W = 10$ cm); neutron production rate dN/dt and total number of neutrons N produced per unit length of the liner.

6 Comparison of 1D simulations with an inverse pinch experiment

An inverse pinch experiment has been carried out at the Institute of High-Current Eelctronics (Tomsk, Russia) [15, 16] using a current pulse amplitude of 850 kA and a high-voltage pulse duration of ~ 80 ns. No bias current was used in the experiment.

Gas was initially localized in an annulus surrounding the inner electrode. It was injected from a Laval nozzle located approximately 1.5 cm from the axis, and the amount of deuterium gas was typically 2.6 μg/cm. Current sheet dynamics were observed with magnetic probes mounted at various radii. Fig. 7(a) compares MHRDR simulations for the Tomsk experimental conditions with data from magnetic probes.

A pulse of neutrons was observed when the accelerated

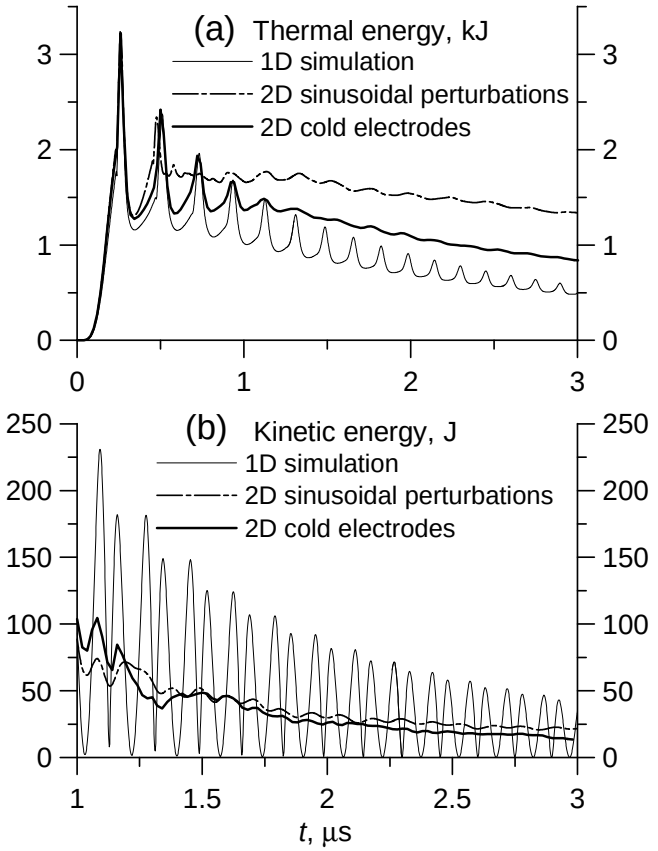

Figure 8: Evolutions of the thermal (a) and kinetic (b) energy of plasma in 1D ($I_b = 25$ kA) and in 2D cases presented in Fig. 9 (perturbations of mass density) and in Fig. 10 (cold electrode as a top boundary in z-direction).

plasma sheet encountered the outer wall. The experiment was designed to generate neutrons when the directed deuterons in the current sheet impacted on the outer wall, which was covered with a layer of deuterated plastic. The directed energy of ions in the current sheet was ~ 4 keV, so neutron emission is not surprising. From an MHD perspective, as described in earlier sections of this paper, directed energy is converted to thermal energy when an accelerated plasma encounters a wall. Fig. 7(b) shows the neutron emission according to MHRDR simulations. The timing of neutrons in the simulation is similar to that reported in the experiment, but the absolute magnitude computed is about one order of magnitude smaller than that reported experimentally. A two–temperature calculation with $T_i > T_e$ would probably give the better agreement because the shock heating affects primarily the ion temperature. The neutrons resulting from thermalization would not depend upon the wall material used. This may help explain why the observed neutron emission appeared about the same even when the wall target material was metal instead of deuterated plastic.

The favorable comparison of simulated data with experimental observations strengthens the point that MHD modeling gives a reasonable description of plasma dynamics despite restrictions due to finite gyro radius and large mean free path.

7 2D modeling of plasma dynamics

The following section describes the results of 2D simulations of an inverse pinch discharge. 2D simulations with uniform distribution of plasma parameters in the axial direction would reproduce 1D plasma dynamics, considered in Section 5. Without axial uniformity 2D hydromagnetic instabilities develop, and some characteristics of plasma dynamics are changed.

Two types of non-uniformity were considered in the simulations. First, a sinusoidal variation of density in the axial direction was considered for a plasma with effectively infinite axial length. In that case, the top and bottom boundaries in the z-direction were treated as surfaces of reflection for density, velocity, temperature, and magnetic field. Second, a realistic zero-temperature conducting boundary was assumed at one end, with a reflecting boundary at the other end. In both simulations the non-uniformities give rise to instability, which evolves in the final equilibrium into turbulent 2D convective cells in the (r, z)-plane.

The simulations in this section were done for $I_b = 25$ kA. With that value of bias current, the 1D model predicts that a substantial amount of plasma stays out of the cold boundary layer leaning on the surface of the outer electrode. Fig. 8 compares the evolution of the thermal and kinetic energies of plasma, normalized to the axial length of the discharge chamber $l_z = 30$ cm, in 1D ($I_b = 25$ kA) and both 2D cases.

7.1 Turbulence generated with the sinusoidal density perturbations

Non-uniformity of current breakdown along the inner electrode may violate the homogeniety of density profile in the axial direction. To study the dynamics of the inverse pinch discharge with seeded sinusoidal perturbations of mass density, a 5% perturbation with axial wavelength of $L_z = 2.5$ cm (exactly two wavelength, 5 cm, between the reflecting boundaries) was imposed upon the initial gas fill in a 3-mm-thick layer near the inner electrode. Plasma dynamics in this case is represented by pressure contours in Fig. 9 at three different times.

Both MHRDR simulations and calculations by snowplow model predict quite a short phase of the effective acceleration during the outward motion of the current sheet for the current pulse shape, given in Fig. 2 [see the relations (10)–(11)]. Most of the time the outward sheet velocity is constant, so the Rayleigh – Taylor (RT) instability does not develope much.

After reflection from the outer wall at $t_1 \approx 240$ ns the shock wave propagates through its own inhomogeneous interface until it reaches the corrugated boundary between the plasma and the magnetic piston at $t_2 \approx 300$ ns. When a

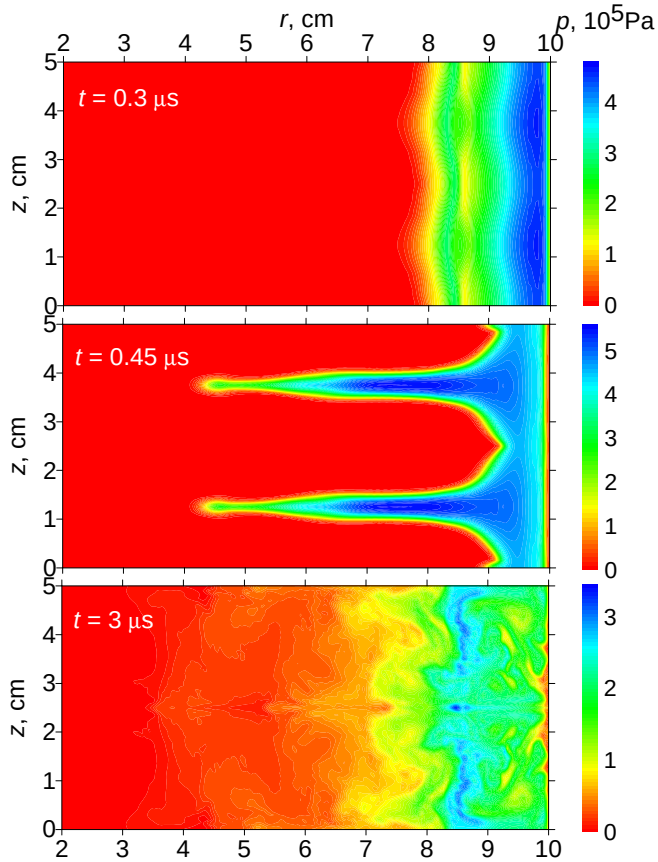

Figure 9: (Color). Pressure level contours p, 10^5 Pa represent plasma dynamics in the case of seeded sinusoidal perturbations of mass density. Three plots shows the consecutive stages of plasma evolution: plasma state after the first bump against the outer electrode $t = 300$ ns, growth of the Rayleigh – Taylor instability $t = 450$ ns and turbulent motion of plasma at $t = 3$ μs.

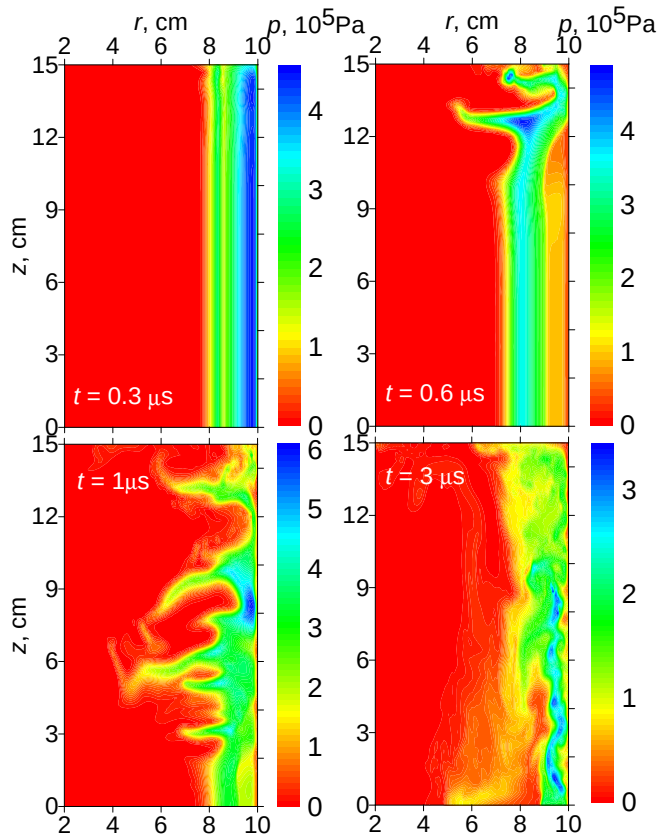

Figure 10: (Color). Pressure level contours p, 10^5 Pa showing plasma dynamics, affected by the presence of the room-temperature electrode at $z = 15$ cm. Reflective boundary is assumed at $z = 0$. Pressure level contours are shown at four consecutive moments: $t = 300$ ns, 600 ns, 1 μs and 3 μs.

shock wave passes through the corrugated contact discontinuity, the turbulence is generated behind the shock wave front due to the development of the Richtmyer – Meshkov (RM) instability. Typical value of the shock wave velocity is of the order of $u \sim (\pi/(t_2 - t_1))\Delta r/2 \approx 3 \times 10^5$ m/s, where Δr has the same meaning as in Eq. (16). Thus one can give a rough estimation of the linear growth rate of RM instability as $\gamma_{RM} \sim 2\pi u/L_z \approx 1/(15 \text{ ns})$.

According to Kadomtsev criterion (19) in 1D simulations an unstable radial pressure profile is formed near the wall at $I_b = 25$ kA. Thus, the outer interface between the plasma and trapped magnetic field is unstable to $m = 0$ interchange mode. The development of this instability may also result in generation of the turbulence.

The amplitude of the effective radial acceleration of both inner and outer interfaces between the plasma and magnetic field can be estimated as $a \sim (\pi/(t_2 - t_1))^2 \Delta r/2 \approx 2 \times 10^{13}$ m/s^2. With this value of acceleration the roughly estimated growth rate of RT instability is of the same order as for RM instability: $\gamma_{RT} \sim \sqrt{2\pi a/L_z} \approx 1/(15 \text{ ns})$. Unlike RM instability, at linear stage the perturbation amplitude of RT instability growth exponentially versus time.

At $t = 1$ μs almost all directed energy of the shock wave has been transferred to the kinetic energy of the convective motion and partially to the thermal energy of plasma (see the plots in Fig. 8). The value of the radial acceleration damps out together with the directed energy of the shock wave. Fig. 9 shows that at $t = 3$ μs plasma settles down into a quasi-equilibrium state with mild-level turbulence, which is characterized by kinetic energy typically a few percents of thermal energy.

7.2 Influence of cold walls

A cold boundary also gives rise to non-uniformities in the axial direction as well as to the RM, RT and interchange modes with qualitative features similar to those described in the last subsection. The electrodes in an actual experiment act as a heat-conducting low-temperature boundary. As a

result of thermal conduction, plasma cools at the surface, pressure drops, and then plasma moves towards the boundary and creates a high-density sheath with approximately uniform pressure. The axial gradients of temperature and density destroy the uniformity of the current sheet because the magnetic field pressure is applied to regions with substantially different Alfven and sound velocities.

Results of simulation are shown in Fig. 10. Pressure contours show a significant disturbance at the zero temperature boundary ($z = 15$ cm) by 0.6 μs. Plasma dynamics at the reflecting boundary ($z = 0$) has the same features as those described in Section 5 until the perturbations arrive to that region at $t \approx 1$ μs. These perturbations propagate in axial direction with the typical velocity of the residual turbulent motion $\sim 2 \times 10^5$ m/s.

8 Discussion

The theoretical investigations described in this paper support the idea that an MTF-relevant inverse-pinch plasma can be generated using the UNR Nevada Terawatt Facility. According to 1D and 2D simulations, and consistent with analytical models, plasma should be formed with temperature over 100 eV, density around 10^{22} m^{-3}, and $\beta \sim 1$. The energy density in the UNR experiments is less than needed for an MTF target, but the regime of collisionality and magnetization is similar. The UNR experiment combined with MAGO results should allow a reasonable assessment of wall confinement for MTF in the inverse-pinch type of configuration.

Because of acceleration during the dynamic formation phase, any type of axial non-uniformity gives rise to the instabilities that have the features of the Rayleigh – Taylor, Richtmyer – Meshkov and $m = 0$ modes. These instabilities resemble the familiar sausage instability of a z-pinch except that $m = 0$ would be stable on the inside of the pressure profile in equilibrium because of favorable field line curvature. The radial acceleration damps out within a few microseconds, and what remains is a mild saturated level of $m = 0$ interchange turbulence.

The Kadomtsev criterion for MHD stability in an equilibrium can be satisfied for $m = 0$ mode if the pressure profile has a sufficiently small gradient in the radial direction. If the pressure profile satisfies the $m = 0$ criterion, then modes with $m = 1$ and larger are stable if $\beta < 0.4$. As noted by Kadomtsev [19], the β requirement is only possible in a z-pinch configuration if a hard core conductor is placed inside the plasma. Otherwise, β goes to infinity on axis where B goes to zero.

An interesting question is how a stable profile might be achieved experimentally in an inverse pinch. We have done many numerical simulations searching for conditions where stable pressure profiles are generated. As discussed in Section 5, particular values of bias current and initial density can be found that generate stable profiles according to 1D simulations, but they do not persist very long in time because the pressure profile changes as the plasma transports heat to the wall. Progress on this issue will be the topic of a future paper.

Effects which have not been considered include ionization and recombination near the walls, wall ablation and sputtering because of the energy flux from the plasma, and the mixing of high-Z impurity ions and their effect upon radiation. Also, thermoelectric terms such as the Nernst current have not been investigated, and two-fluid effects such as Hall terms have not been included, although some versions of the MHRDR code have that capability.

The main interest at present is to determine whether plasma parameters in an experiment with existing hardware at UNR would create physical conditions relevant to MTF. The agreement between our analytic estimates and numerical results, combined with the favorable comparison between MHRDR modeling and experimental data from the inverse pinch at Tomsk, provides us confidence with the MHD model. We conclude from this work that an experiment at UNR would make a useful contribution to the search for a suitable MTF target plasma.

9 Acknowledgments

Authors greatly appreciate numerous stimulating discussions with Prof. Tom Cowan and administrative support of Dr. Nathalie Le Galloudec.

This work has been sponsored by DOE NNSA/NV Cooperative Agreement DE-FC08-01NV15050.

References

[1] D. D. Ryutov, D. C. Barnes, B. S. Bauer, J. H. Hammer, C. W. Hartman, R. C. Kirkpatrick, I. R. Lindemuth, V. Makhin, P. B. Parks, D. B. Reisman, P. T. Sheehey, and R. E. Siemon, Nuclear Fusion **43**, 955 (2003).

[2] R. C. Kirkpatrick, I. R. Lindemuth, and M. S. Ward, Fusion Technology **27**, 201 (1995).

[3] D. D. Ryutov and R. E. Siemon, Comments Plasma Phys. Controlled Fusion, Comments on Modern Physics **2**, C185 (2001).

[4] R. P. Drake, J. M. Hammer, C. W. Hartman, L. J. Perkins, and D. D. Ryutov, Fusion Technology **30**, 310 (1996).

[5] G. E. Vekshtein, *Magnetothermal processes in dense plasmas*, in Reviews of Plasma Physics, edited by B. B. Kadomtsev, Consultants Bureau, New York, Vol. 15, 1 (1990).

[6] I. R. Lindemuth, J. S. Pettibone, J. C. Stevens, R. C. Harding, D. M. Kraybill, and L. J. Suter, Phys. Fluids **21**, 1723 (1978).

[7] B. Feinberg, Plasma Phys. **18**, 265 (1976).

[8] I. R. Lindemuth, R. E. Reinovsky, R. E. Chrien, J. M. Christian, C. A. Ekdahl, J. H. Goforth, R. C. Haight, G. Idzorek, N. S. King, R. C. Kirkpatrick, R. E. Larson, G. L. Morgan, B. W. Olinger, H. Oona, P. T. Sheehey, J. S. Shlachter, R. C. Smith, L. R. Veeser, B. J. Warthen, S. M. Younger, V. K. Chernyshev, V. N. Mokhov, A. N. Demin, Y. N. Dolin, S. F. Garanin, V. A. Ivanov, V. P. Korchagin, O. D. Mikhailov, I. V. Morozov, S. V. Pak, E. S. Pavlovskii, N. Y. Seleznev, A. N. Skobelev, G. I. Volkov, and V. A. Yakubov, Phys. Rev. Lett. **75**, 1953 (1995).

[9] B. S. Bauer, V. L. Kantsyrev, F. Winterberg, A. S. Shlyaptseva, R. C. Mancini, H. Li, and A. Oxner, The dense Z-pinch program at the University of Nevada, Reno, The 4-th International conference on dense z-pinches: Vancouver, Canada: 28-31 May 1997, AIP Conference Proceedings, 1997, Volume 409, pp. 153-156.

[10] O. A. Anderson, H. P. Furth, J. M. Stone, and R. E. Wright, Phys. Fluids **1**, 489 (1958).

[11] A. L. Hoffman, J. Plasma Physics **1**, 193 (1967).

[12] F. Y. Sorrell, Phys. Fluids **11**, 993 (1968).

[13] R. L. Burton and P. J. Turchi, J. of Propulsion and Power **14**, 716 (1998).

[14] A. F. Aleksandrov and A. A. Rukhadze, Sov. Phys.-Usp. **17**, 44 (1974).

[15] V. M. Bystritsky, V. M. Grebenyuk, S. S. Parzhitsky, F. M. Pen'kov, V. A. Stolupin, G. A. Mesyats, V. I. Makhrin, N. A. Ratakhin, V. A. Sinebryukhov, E. N. Volkov, Vit. M. Bystritskii, M. Filipovicz, J. Wozniak, E. Gula, G. N. Dudkin, B. A. Nechaev, and V. N. Padalko, Nucl. Instrum. Methods Phys. Res. A **455**, 706 (2000).

[16] Vit. M. Bystritskii, V. M. Bystritsky, J. Wozniak, V. M. Grebenyuk, E. Gula, G. N. Dudkin, G. A. Mesyats, B. A. Nechaev, V. N. Padalko, S. S. Parzhitsky, F. M. Pen'kov, N. A. Ratakhin, S. A. Sorokin, and V. A. Stolupin, Techn. Phys. **47**, 1098 (2002).

[17] P. H. Rebut and A. Torossian, Plasma Physics **5**, 133 (1963).

[18] J. Adam, F. Alvarez de Toledo, P. H. Rebut, and A. Torossian, Plasma Physics **11**, 297 (1969).

[19] B. B. Kadomtsev, *Hydromagnetic stability of a plasma*, in Reviews of Plasma Physics, edited by M. A. Leontovich, Consultants Bureau, New York, Vol. 2, 153 (1966).

[20] D. W. Scudder, J. S. Shlachter, J. E. Hammel, F. Venneri, R. Chrien, R. Lovberg, and R. Riley. In Physics of Alternative Magnetic Confinement Schemes, S. Ortolani, E. Srodoni (Eds). SIF, Bologna (1991), p. 519.

[21] SCREAMER - A Pulsed Power Design Tool developed at SNL by M. L. Kiefer, K. L. Fugelso, K. W Struve, and M. M. Widner.

[22] S. I. Braginskii, *Transport Processes in a Plasma*, in Review of Plasma Physics, edited by M. A. Leontovich Consultants Bureau, New York, Vol. 1, 205 (1965).

[23] K. F. McKenna and T. M. York, Plasma Physics **17**, 1 (1975). T. M. York and K. F. McKenna RSI **44**, 588 (1973).

[24] U. Shumlak, R. P. Golingo, B. A. Nelson, D. J. Den Hartog, Phys. Rev. Lett. **87**, 205005 (2001); U. Shumlak, B. A. Nelson, R. P. Golingo, S. L. Jackson, E. A. Crawford, and D. J. Den Hartog, Phys. Plasmas **10**, 1683 (2003).

[25] V. I. Sotnikov, I. Paraschiv, V. Makhin, B. S. Bauer, J. N. Leboeuf, and J. M. Dawson, Phys. Plasmas **9**, 913 (2002).

[26] P. V. Sasorov and N. A. Bobrova, Sov. J. Plasma Phys. **16**, 229 (1990).

[27] A. A. Esaulov and P. V. Sasorov, Plasma Phys. Rep. **23**, 576 (1997).